Electronic Supplementary Material (ESI) for Chemical Science.

Supplementary Information

Participation of Electrochemically Inserted Protons in the Hydrogen Evolution Reaction on Tungsten Oxides

Michael A. Spencer,[a] Noah P. Holzapfel,[a] Kyung-Eun You,[b] Giannis Mpourmpakis,[b] Veronica Augustyn[a,*]

[a]Department of Materials Science and Engineering, North Carolina State University, 911 Partners Way, Raleigh, NC 27606, USA

[b]Department of Chemical and Petroleum Engineering, University of Pittsburgh, Pittsburgh, PA 15260, USA

*corresponding author: vaugust@ncsu.edu

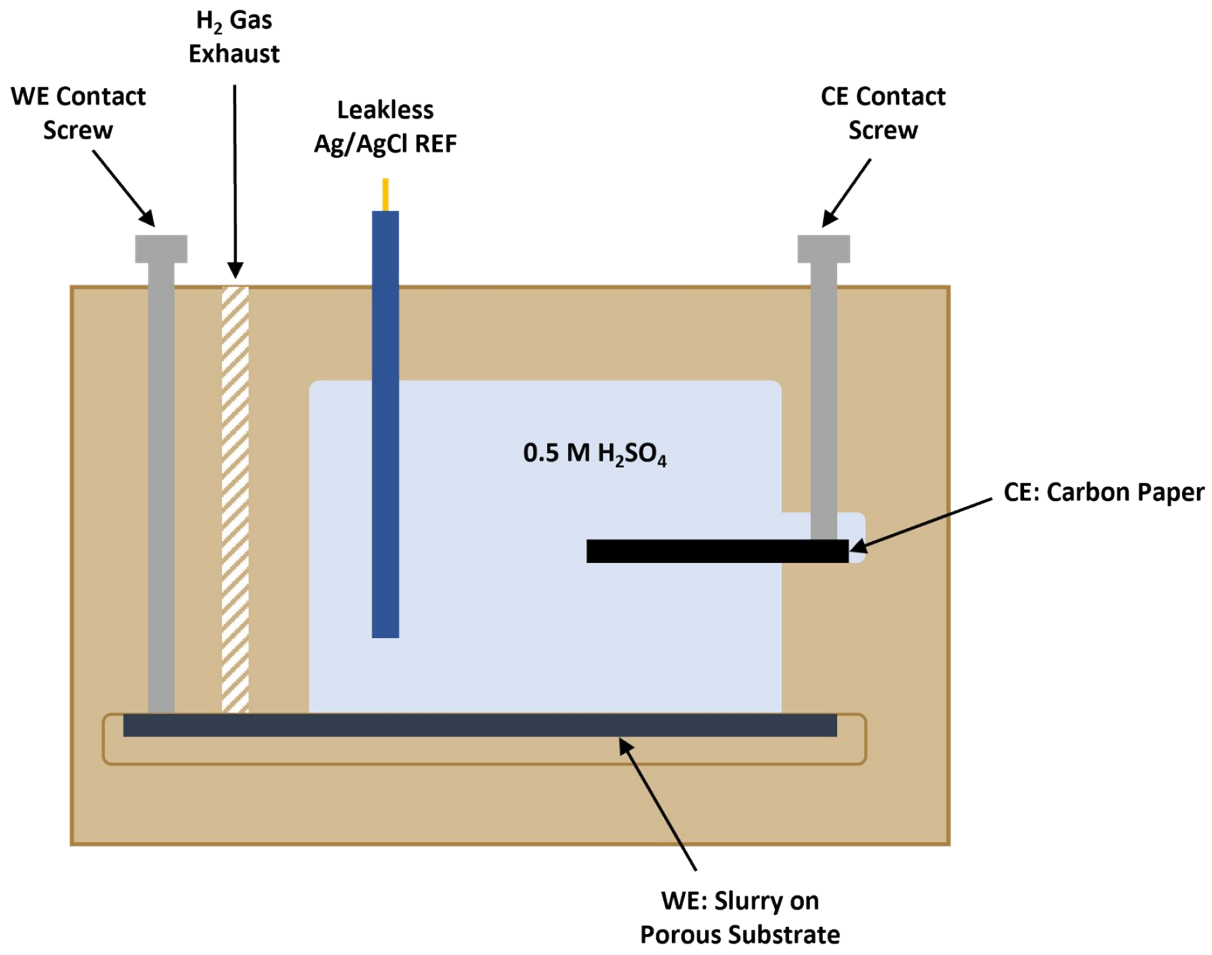

Figure S1. Schematic of the operando electrochemical cell used to collect synchrotron XRD patterns. The body of the cell (tan component) was made of PTFE. A slurry electrode containing the active material of interest was used as the working electrode (WE) and it laid flat on the bottom of the cell. An extra open port served as the exhaust for evolved hydrogen gas. The reference electrode (REF) was a leakless Ag/AgCl reference electrode, and the counter electrode (CE) was porous carbon paper. The electrolyte was 0.5 M H_2SO_4. Two coated screws were used for electrical contact to the WE and CE. The cell was sealed using rubber gaskets and Kapton films that were pinched between the PTFE and stainless steel plates (not shown). This operando XRD cell is based on a design reported in a previous study.[1]

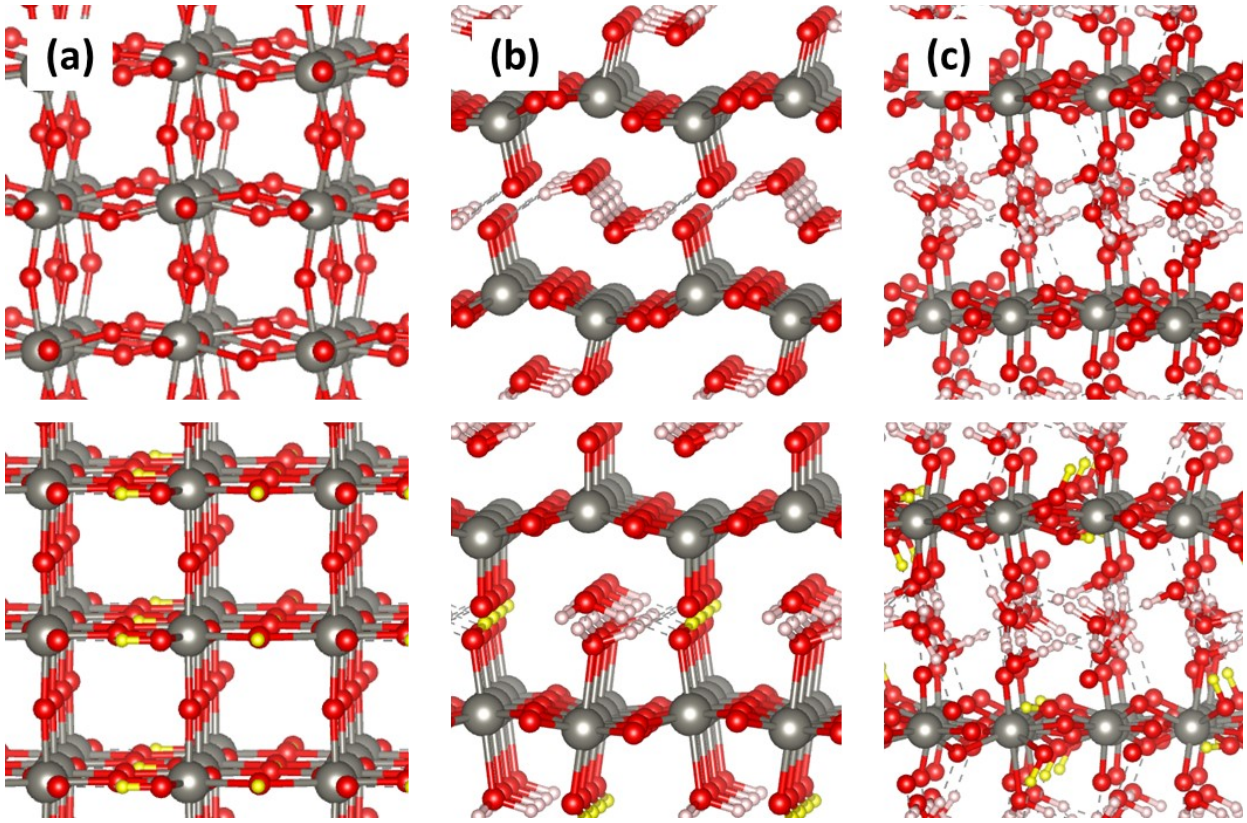

Figure S2. Optimized structures of pristine (top) and protonated (bottom) (a) WO_3, (b), $WO_3 \cdot H_2O$ and (c) $WO_3 \cdot 2H_2O$. The ratio of H to W is maintained as 0.5 in the protonated structures (bottom panels). Inserted protons are color-coded in yellow.

Table S1. Lattice constants of tungsten oxides with and without proton insertion. Comparative analysis between computational results obtained at r^2SCAN+rVV10 level of theory.

		WO_3		**$WO_3 \cdot H_2O$**		**$WO_3 \cdot 2H_2O$**	
		Pristine (monoclinic)	$H_{0.5}WO_3$ (cubic)	Pristine	$H_{0.5}WO_3 \cdot H_2O$	Pristine	$H_{0.5}WO_3 \cdot 2H_2O$
Lattice constants	a	7.330	3.746	5.205	5.340	10.266	10.403
	b	7.433	3.791	10.356	10.096	13.382	13.025
	c	7.692	3.776	5.119	5.311	10.454	10.676

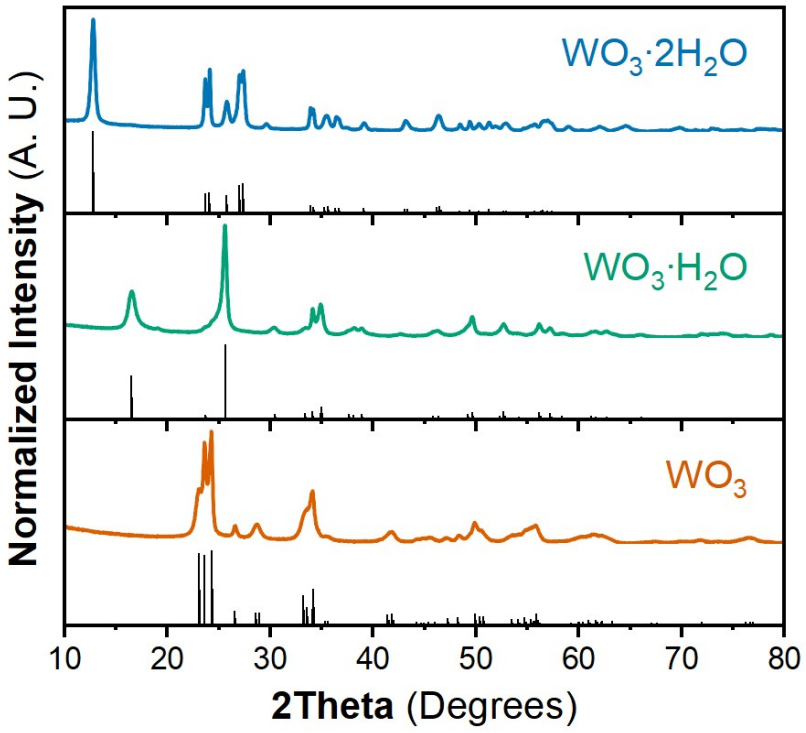

Figure S3. Powder XRD patterns of WO_3, $WO_3 \cdot H_2O$, and $WO_3 \cdot 2H_2O$ using a Cu $K\alpha_1/K\alpha_2$ X-ray source (λ = 1.5406 Å/1.5444 Å). Calculated reference patterns were adapted from the structures reported previously.[2–4]

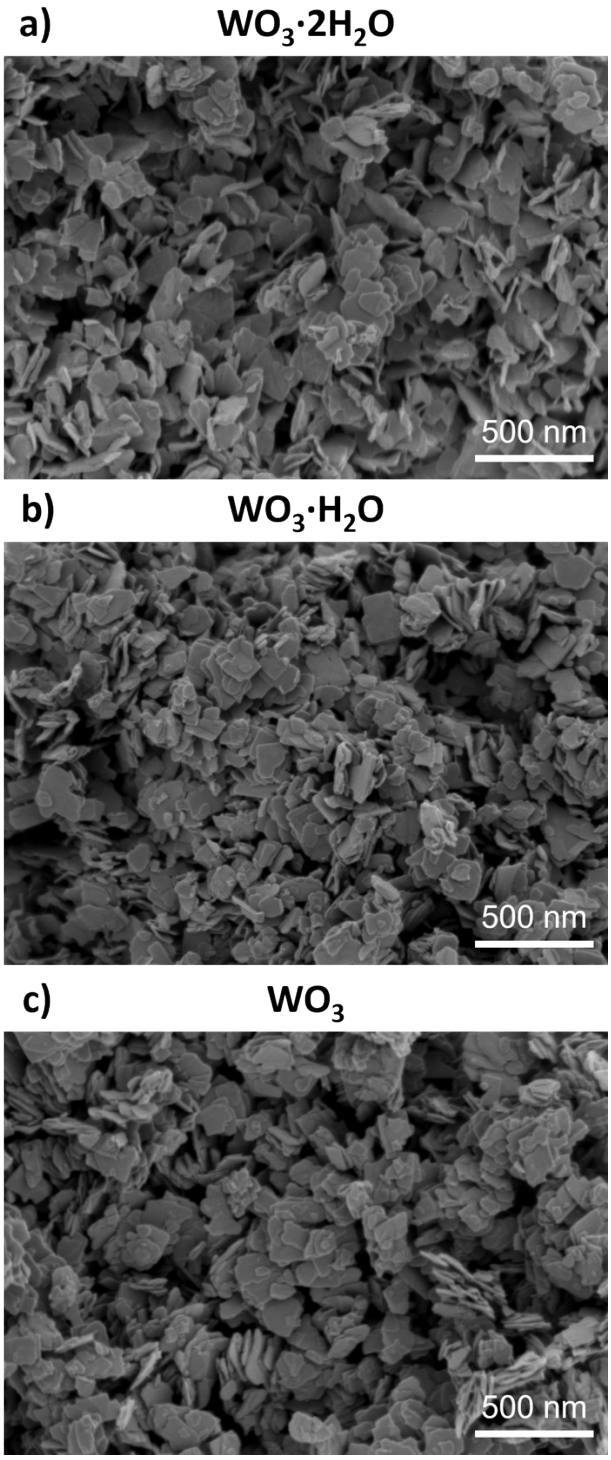

Figure S4. SEM of (a) acid-precipitated $WO_3 \cdot 2H_2O$ and thermally de-hydrated (b) $WO_3 \cdot H_2O$ (120°C), and (c) WO_3 (350°C).

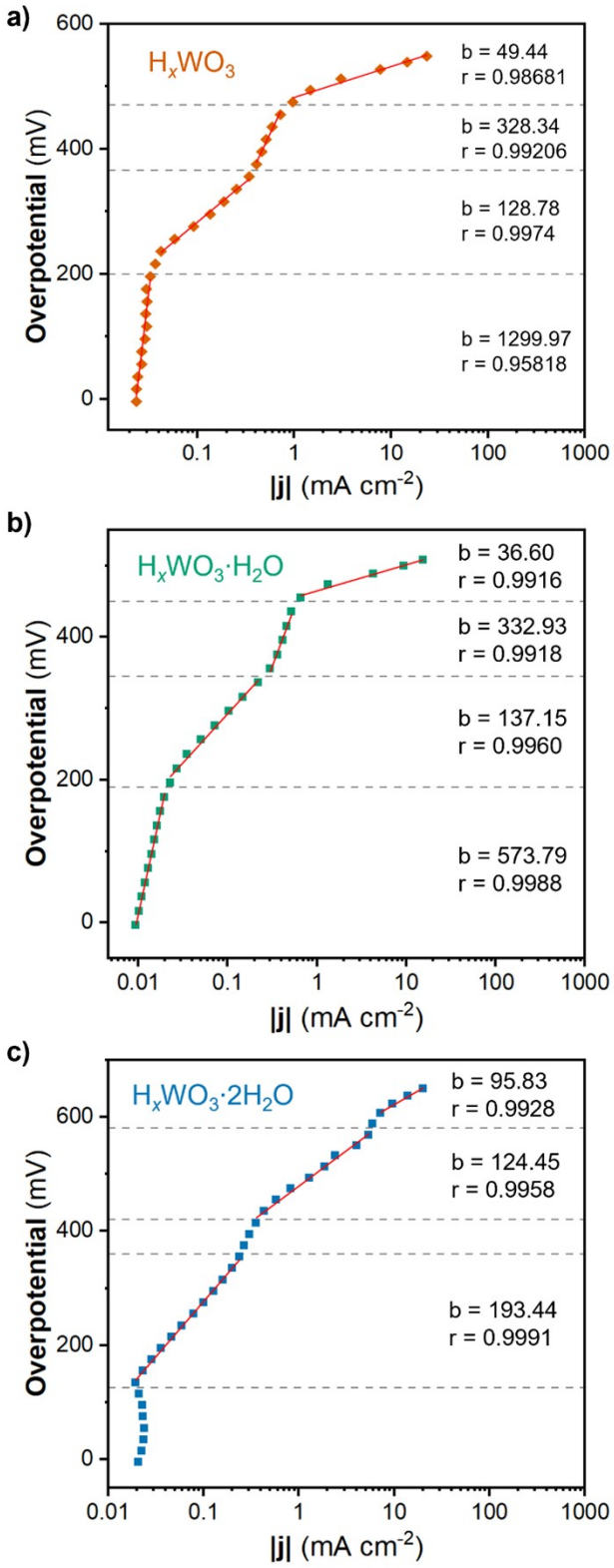

Figure S5. Tafel slopes calculated for (a) H_xWO_3, (b) $H_xWO_3 \cdot H_2O$, and (c) $H_xWO_3 \cdot 2H_2O$.

Table S2: Comparison of tungsten oxides with the electrocatalytic properties of various non-precious metal-based materials, as well as commercial Pt/C, towards the HER in acidic electrolytes.

Material	**Electrolyte**	**Mass Loading** (mg/cm^2)	**Overpotential @ 10 mA cm^{-2}** (mV)	**Tafel Slope** (mV/dec)	**Ref**
Pt/C	0.5 M H_2SO_4	0.1	18.2	30	5
MoS_2 (nano)	0.5 M H_2SO_4	-	150-200	50	6
$Li_{0.29}MoS_2$	0.1 M H_2SO_4	0.35	~165	74	7
$LiMoS_2$	0.1 M H_2SO_4	0.35	~240	112	7
CoS_2	0.5 M H_2SO_4	-	190	51	8
CoPS (film)	0.5 M H_2SO_4	-	128	57	9
CoPS (nano)	0.5 M H_2SO_4	-	48	56	9
WO_3	0.5 M H_2SO_4	0.285	637	120	10
H_xWO_3	0.5 M H_2SO_4	0.1	532	49	This Work
$H_xWO_3{\cdot}H_2O$	0.5 M H_2SO_4	0.1	501	37	This Work
$H_xWO_3{\cdot}2H_2O$	0.5 M H_2SO_4	0.1	622	96	This Work
$WO_{2.9}$	0.5 M H_2SO_4	0.285	70	50	10
MoO_3	0.1 M H_2SO_4	0.2	422	146	11
MoO_{3-y}	1 M H_2SO_4	-	201	90	12
TiO_2	0.5 M H_2SO_4	0.255	550 (8.3 mA cm^{-2})	-	13
α-Ti_2O_3	0.5 M H_2SO_4	-	495	241	14
o-Ti_2O_3	0.5 M H_2SO_4	-	442	232	14
γ-Ti_2O_3	0.5 M H_2SO_4	-	271	199	14

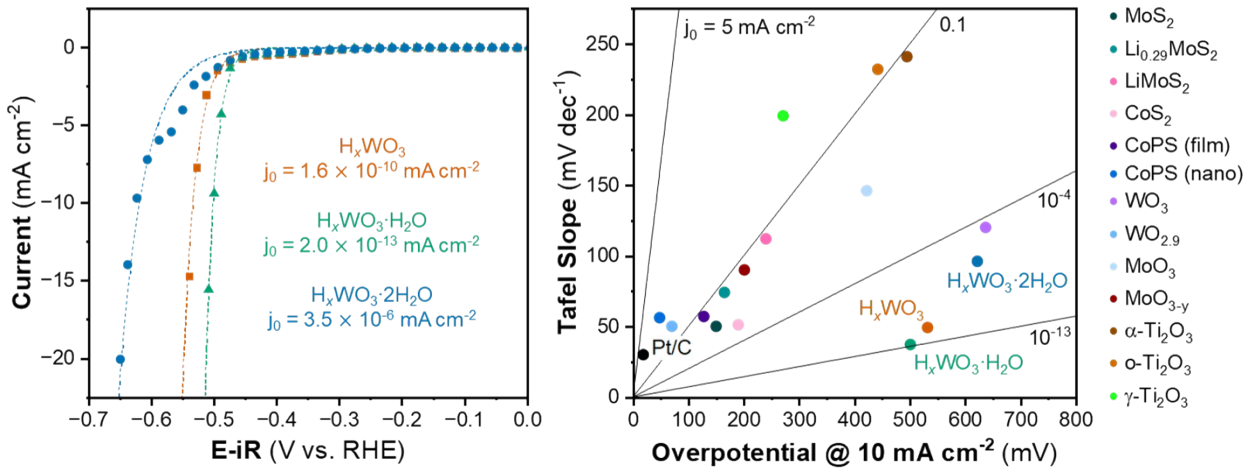

Figure S6. (a) Chronoamperometric data (scatter plot) and calculated current response (dashed lines) for each catalyst studied in this work based on the Tafel equation ($\eta = b\log(j/j_0)$; where η is overpotential, b is Tafel slope, j is current density, and j_0 is exchange current density). (b) Plot of Tafel slope vs. overpotential for Pt/C, a variety of non-precious metal catalysts (data obtained from references listed in **Table S2**), and the $H_xWO_3{\cdot}nH_2O$ materials investigated in this work, with lines representing trends in exchange current density (j_0) calculated from the Tafel equation.

Discussion 1. Calculating proton composition

Choosing which technique is best suited for calculating the proton composition is important. When parasitic or electrocatalytic reactions are present in the cathodic sweep of cyclic voltammetry, the anodic capacity is often used to quantify the amount of ions inserted into a material. However, small negative charge contributions from the HER (Q_{HER}) can contribute to the measured current during cathodic and anodic scans, even at potentials prior to reaching the overpotential required to reach 10 mA cm^{-2}. The three methods we investigated to calculate the charge associated with insertion (Q_{insert}) and the proton composition of protonated tungsten oxides were: (1) integration of the anodic current vs. time from RDE CV measurements of thin films on glassy carbon, (2) $Q\text{-}Q_0$ capacities with irreversible charge subtraction from RDE CV measurements, (3) and $Q\text{-}Q_0$ capacities with irreversible charge subtraction CVs of high mass loading slurry electrodes.

Method 1 and 2 use the cyclic voltammetry data obtained from the RDE setup with a rotation rate of 1600 rpm and a scan rate of 10 mV s^{-1}. To calculate the capacity using Method 1, the integral is taken of the positive current region with respect to time (**Equation S1**) for one cycle and converted to the number of electrons per tungsten.

$$Q = \int i dt \qquad \text{(S1)}$$

The proton insertion capacities calculated from cyclic voltammetry at 10 mV s^{-1} using Method 1 resulted in the following pre-HER compositions: $H_{0.18}WO_3$, $H_{0.26}WO_3{\cdot}H_2O$, and $H_{0.21}WO_3{\cdot}2H_2O$ (**Table S3)**. The compositions calculated using Method 1 are underestimates of the true proton composition within the structure due to the current contribution from the HER.

To correct for the low magnitude HER current contributions observed in a limited potential window, we employed a charge correction across multiple cyclic voltammetry cycles. To perform composition measurements as a function of time and potential, the overall charge stored (recorded in the EC-Lab software) was plotted as a function of time. To account for charge

associated with irreversible reactions, a linear fit was applied to the local maxima in the Q vs. t curve that was subsequently subtracted from the overall Q-Q_0 curve. This method assumes that the irreversible charge contribution is equal across multiple CV cycles. After the linear subtraction, the local maxima return to ~0 C, therefore a second assumption is required that all inserted protons can be extracted during the anodic scan.

The charge correction approach applied to CV data from RDE electrodes is defined as Method 2. The proton compositions calculated using Method 2 were higher for each material: $H_{0.24}WO_3$, $H_{0.54}WO_3{\cdot}H_2O$, and $H_{0.32}WO_3{\cdot}2H_2O$ (**Table S3**), suggesting that it is an effective method to account for low current magnitude parasitic reactions in well-understood systems where capacity loss is not attributed to the material itself. This method also provides an approach to track the composition as a function of potential, as shown in **Figure 4** of the main text.

Method 3 applies the charge correction approach to high mass loading slurry electrodes on carbon paper substrates. A high mass loading slurry electrode can exhibit slower kinetics compared to thin film electrodes on glassy carbon, however, the advantage of using a high mass loading electrode is that the current due to insertion (Q_{insert}) far exceeds the low magnitude charge contribution from HER (Q_{HER}) at potentials preceding the HER onset for the tungsten oxides. The reason $Q_{insert} >> Q_{HER}$ is twofold: (1) upon increasing the mass loading of the relatively low surface area tungsten oxides leads to the addition of more proton storage sites compared to active HER sites, and (2) the slurry electrode microstructure and stationary positioning lead to less favorable removal of hydrogen gas during the HER, thus we expect slower kinetics compared to the RDE setup. An example of the charge correction approach applied using Method 3 on 6 mg cm^{-2} slurry electrode of $WO_3{\cdot}H_2O$ on CP is shown in **Figure S7**. The following compositions were observed using Method 3: $H_{0.55}WO_3$ (10 mV s^{-1}), $H_{0.65}WO_3$ (1 mV s^{-1}), $H_{0.69}WO_3{\cdot}H_2O$ (10 mV s^{-1}), and $H_{0.47}WO_3{\cdot}2H_2O$ (10 mV s^{-1}). These compositions provided the most reasonable proton compositions in agreement with prior literature and expected structural transformations (as addressed in **Discussion 2**). These compositions are represented in **Figure 5** of the main text

and used as the closest approximation of the proton composition attainable leading up to the onset of HER activity.

Table S3. Comparison of proton compositions for each material calculated by integrating the current vs. time curve from thin film RDE electrodes in a limited potential window (Method 1), applying a $Q\text{-}Q_0$ correction to the results from RDE electrodes (Method 2), and using the $Q\text{-}Q_0$ correction approach on slurry electrodes with a wider potential window and a sweep rate of 10 mV s^{-1} where $Q_{insert} >> Q_{HER}$ (Method 3).

Material	Method 1	Method 2	Method 3
WO_3	0.18	0.24	0.55
$WO_3 \cdot H_2O$	0.26	0.54	0.69
$WO_3 \cdot 2H_2O$	0.21	0.32	0.47

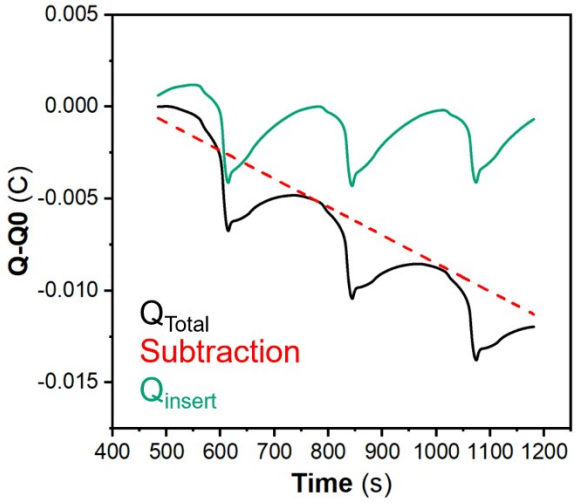

Figure S7. Charge correction protocol applied to the results from a 6 mg cm^{-2} slurry electrode of $WO_3 \cdot H_2O$ on CP that was cycled using CV at a scan rate of 10 mV s^{-1}.

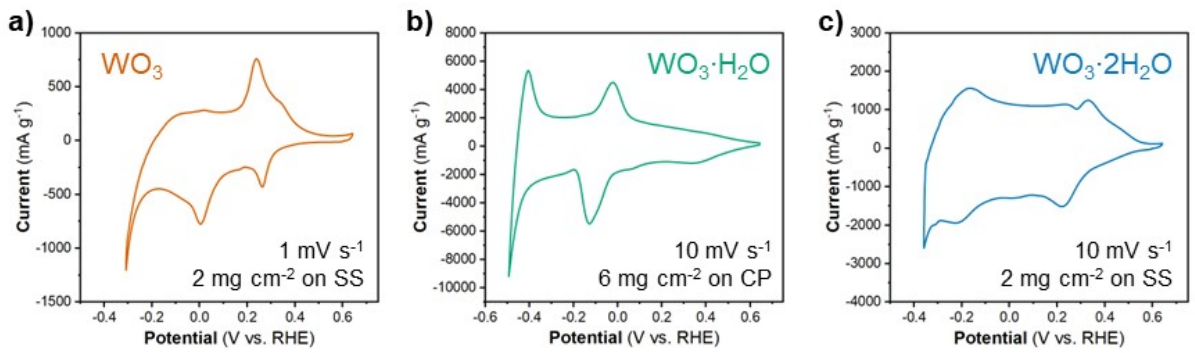

Figure S8. Cyclic voltammetry results obtained during the operando XRD measurements of (a) a 2 mg cm^{-2} WO_3 slurry electrode on stainless steel with a scan rate of 1 mV s^{-1}, (b) a 6 mg cm^{-2} $WO_3 \cdot H_2O$ slurry electrode on carbon paper with a scan rate of 10 mV s^{-1}, and (c) a 2 mg cm^{-2} $WO_3 \cdot 2H_2O$ slurry electrode on stainless steel with a scan rate of 10 mV s^{-1}.

Discussion 2.

WO_3

The structure of the anhydrous WO_3 is well established, crystallizing with monoclinic $P2_1/n$ space group symmetry consisting of octahedral tilts of the pattern ($a^-b^+c^-$) in Glazer notation and antiparallel displacements of the W^{6+} ions within the octahedra due to second-order Jahn-Teller effects. **Figure 6** in the main text shows the diffraction patterns and corresponding potential and current as a function of time for WO_3 during cyclic voltammetry in 0.5 M H_2SO_4 at 1 mV s^{-1}. After the first proton insertion event with a peak potential (E_p) of 0.26 V vs. RHE, the peaks originally associated with the (002), (020), and (200) indices of the monoclinic cell at 10.84, 11.14, and 11.40 degrees 2θ, respectively, merge into two peaks suggesting a transition to higher symmetry. The 1D XRD pattern collected at 0.177 V (vs. RHE) can be well fit by the structure reported for $H_{0.23}WO_3$ determined from X-ray and neutron diffraction studies performed by Dickens and Hurditch.[15] $H_{0.23}WO_3$ has tetragonal $P4/nmm$ space group symmetry with no observable tilting of the octahedra while the antiparallel displacements of W^{6+}-ions remain. After the second proton insertion event at E_p = 0.0 V vs. RHE, the (100) and (110) reflections positioned at 10.76 and 11.29 degrees 2θ, respectively, merge into a single peak suggesting another transition to higher symmetry. The 1D pattern collected under an applied potential of -0.35 V (vs. RHE) matches well with the structure of $H_{0.5}WO_3$ previously reported by Glemser and Naumann.[16] $H_{0.5}WO_3$ was reported to have a cubic unit cell with $Pm\bar{3}m$ space group symmetry (a = 3.75 Å) via X-ray diffraction. The perovskite-like structure does not demonstrate any observable tilts, nor does it allow for the displacement of the W^{6+}-ion. A separate report by Wiseman and Dickens utilized neutron diffraction on a deuterated analogue ($D_{0.53}WO_3$) and observed weak supercell reflections that are consistent with a cubic cell with $Im\bar{3}$ space group symmetry (a = 7.562 Å or $a/2$ = 3.781 Å).[17] The $Im\bar{3}$ structure is a tilted derivative of the archetypical perovskite structure with the tilting scheme ($a^+a^+a^+$) in Glazer notation.[18] The structure determined from neutron diffraction is of high

fidelity due to the higher sensitivity of the measurement with respect to oxygen and deuterium positions. We do not observe the supercell reflections consistent with the $Im\bar{3}$ structure and have opted to perform Pawley refinements with the smaller $Pm\bar{3}m$ unit cell determined from X-ray diffraction. Our data matches well with the previous reports (a = 3.7935(1)). It should also be mentioned that Pawley refinements with both the $Pm\bar{3}m$ model and $Im\bar{3}$ model resulted in similar fits to the data. **Figure 7** in the main text shows the proton composition and pseudo-cubic a-lattice parameter (a_p) calculated from the lattice parameters of each phase (**Equation S2-S4**) as a function of potential. After the pure cubic structure forms, a_p continues to increase from 3.770 Å at -0.083 V to 3.787 Å at -0.282 V vs. RHE. The same series of transitions occurred in reverse order as protons de-inserted during the anodic cyclic voltammetry scan from -0.31 V to 0.64 V vs. RHE.

Monoclinic: $$a_p = \frac{(a+b+c)}{6} \quad \text{(S2)}$$

Tetragonal: $$a_p = \frac{(2a/\sqrt{2})+c}{3} \quad \text{(S3)}$$

Cubic: $$a_p = a \quad \text{(S4)}$$

$WO_3 \cdot H_2O$

The structure of $WO_3 \cdot H_2O$ was reported previously by Szymanski and Roberts as a primitive orthorhombic cell with *Pmnb* (non-standard setting of *Pnma*) space group symmetry and lattice parameters of a = 5.249(2) Å, b = 10.711(5) Å, and c = 5.133(2) Å.[2] A separate report by Lalik et al. utilized neutron diffraction and scattering techniques in combination with DFT calculations to demonstrate the true structure of $WO_3 \cdot D_2O$ has $P2_12_12_1$ space group symmetry with a = 10.654(1) Å, b = 5.2486(6) Å, and c = 5.1474(5) Å.[19] The difference between these two cells consists of changes in the orientation of the water molecule within the framework as well as the presence of a small θ-tilt (in Aleksandrov notation) perpendicular to the layer plane. The minute discrepancies

between these reports may be attributed to the different techniques used to determine the structure, single-crystal XRD (Syzmanski) and NPD (Lalik), the latter being more sensitive to both oxygen and deuterium positions. Lalik et al. further demonstrated that there were no observable structural transitions over the temperature range 1.5 K to 300 K. Pawley refinements of our diffraction data can be fit well with both models. While we admit the structure with $P2_12_12_1$ space group symmetry may be the more correct assignment, the minute differences were not apparent in our experiments. We elected to model the data with the *Pmnb* cell due to the higher symmetry of the cell although it should be mentioned that Pawley refinements with both structural models resulted in identical fits to the data. While multiple proton insertion events are observed in the CV, our data does not indicate any structural transitions associated with these events. Instead, the data can be modeled by a contraction of the interlayer distance and an expansion of the inorganic plane. Further studies with neutron diffraction may be necessary to elucidate the true structures of the $H_xWO_3 \cdot H_2O$. We speculate based on group theory that the series of transitions may follow the series $P2_12_12_1 \rightarrow Pmnb \rightarrow Cmcm \rightarrow I4/mmm$. These transitions are associated with a loss of θ-tilts, then a loss of the in-plane ϕ-tilts, and finally the loss of the W^{6+}-cation displacements. These structural phase transitions are consistent with other layered perovskite-like materials with the Ruddlesden-Popper structure.[20] The mode of transitions (i.e. loss of tilting and ion displacements) would be similar to what is observed in the H_xWO_3 system where tilting is lost before the cation displacements.

$WO_3 \cdot 2H_2O$

The structure of $WO_3 \cdot 2H_2O$ was reported by Li et al. in 2000 from powder XRD. It has a monoclinic cell with $P2_1/n$ symmetry with a complex pattern of octahedral tilting.[3] During electrochemical proton insertion, operando XRD results (**Figure 10a**) show that the $(20\bar{2})$ and (202) reflections at 11.16 and 11.34 degrees 2θ, respectively, merge as the potential is scanned from 0.642 V to -

0.05 V vs. RHE, and they proceed to split at higher proton compositions between -0.05 V and -0.358 V vs. RHE. Furthermore, the (020) peak position remains constant, indicating that the interlayer spacing does not change during proton (de)insertion. This trend is also observed with the $(22\bar{2})$ and (222) reflections at 12.70 and 12.88 degrees 2θ, respectively. The opposite transitions occur during deprotonation in the anodic scan of the CV. Pawley refinements were performed on 1D diffraction patterns of the full 2θ range recorded during the operando measurements of $WO_3 \cdot 2H_2O$. All of the collected diffraction patterns could be modeled with the monoclinic $P2_1/n$ structure with changes in the *a*- and *c*- lattice parameters, with the most significant change in the *a*-axis (**Figure 11**). Overall, these results indicate that upon proton insertion and de-insertion in $H_xWO_3 \cdot 2H_2O$, the structural transitions are limited to the *ac*-plane and may be associated with changes in the degree of tilting and changes in bond lengths within the inorganic layers.

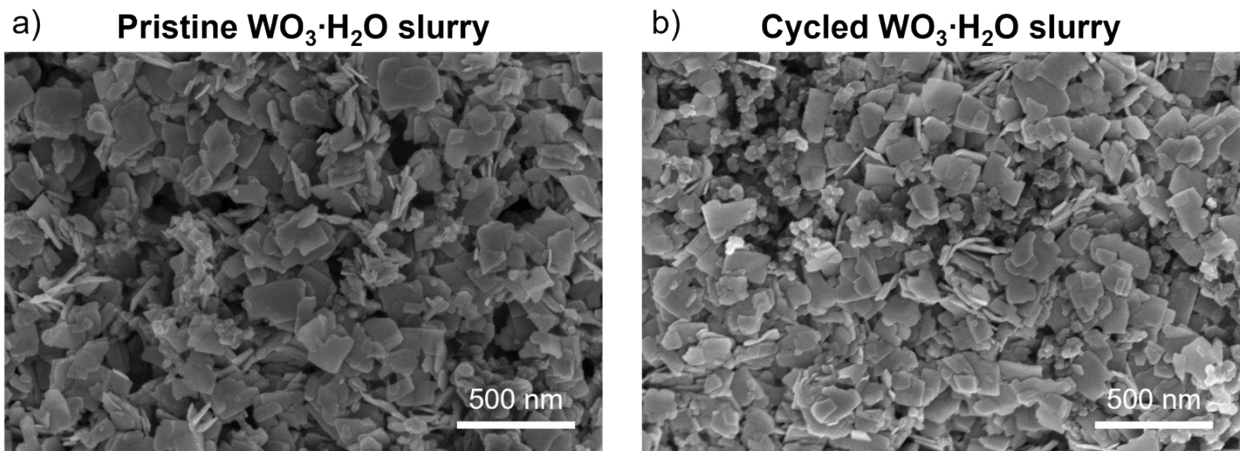

Figure S9. Scanning electron microscopy images of a 6 mg cm^{-2} $WO_3 \cdot H_2O$ slurry electrode (a) before and (b) after cyclic voltammetry in 0.5 M H_2SO_4 with a lower cutoff potential of -0.8 V vs. RHE.

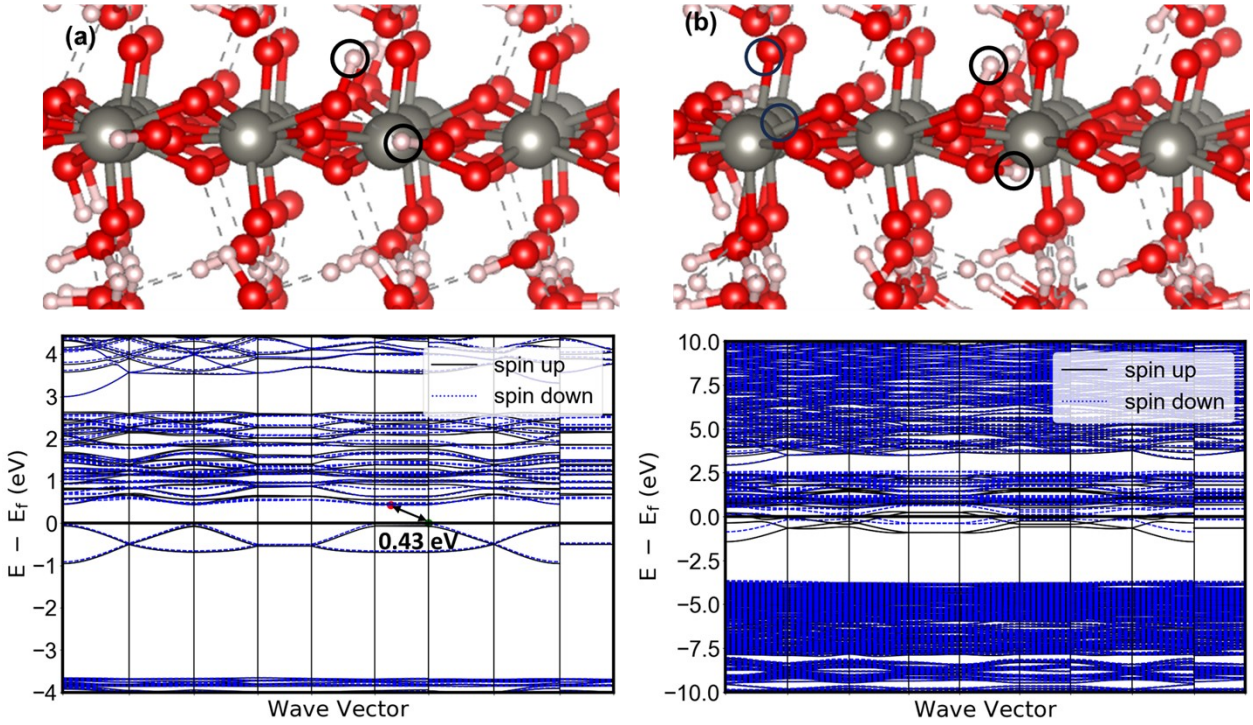

Figure S10. The geometry and band structure of two thermodynamically competitive (< 0.001 eV energy difference) configurations ((a) and (b)) of $H_{0.5}WO_3 \cdot 2H_2O$.

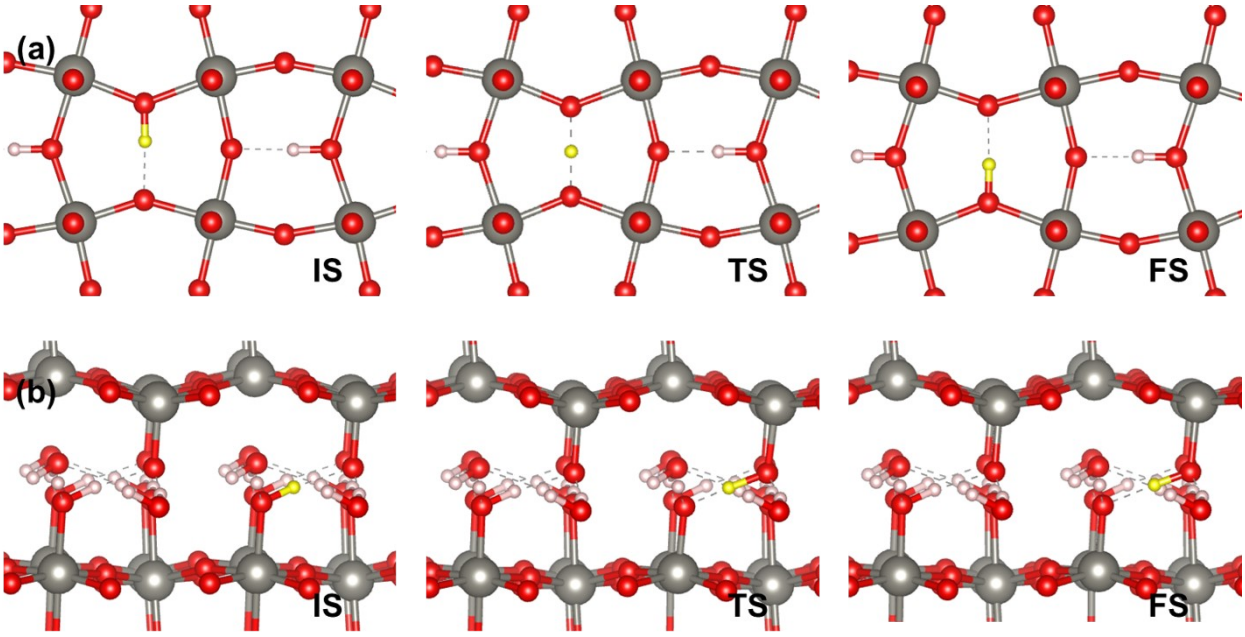

Figure S11. Structural configuration of initial (IS), transition (TS), and final states (FS) of proton conduction in the bulk of (a) $H_{0.5}WO_3$ and (b) $H_{0.5}WO_3 \cdot H_2O$. The free energy of activation barriers at room temperature are 0.00 eV and 0.14 eV, respectively. Diffusing protons are color-coded in yellow.

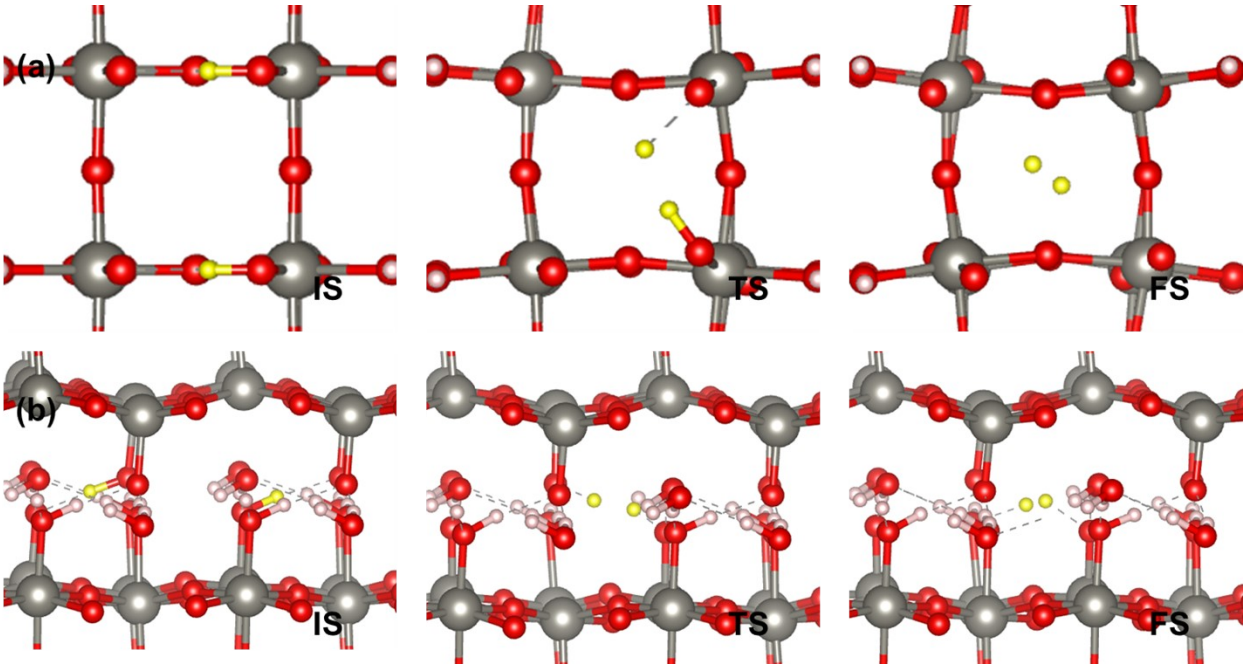

Figure S12. Structural configuration of initial (IS), transition (TS), and final states (FS) of hydrogen formation in the bulk of (a) $H_{0.5}WO_3$ and (b) $H_{0.5}WO_3 \cdot H_2O$. The free energy of activation barriers are 2.25 eV and 1.98 eV at room temperature, respectively. Hydrogens involved in H_2 formation are color-coded in yellow.

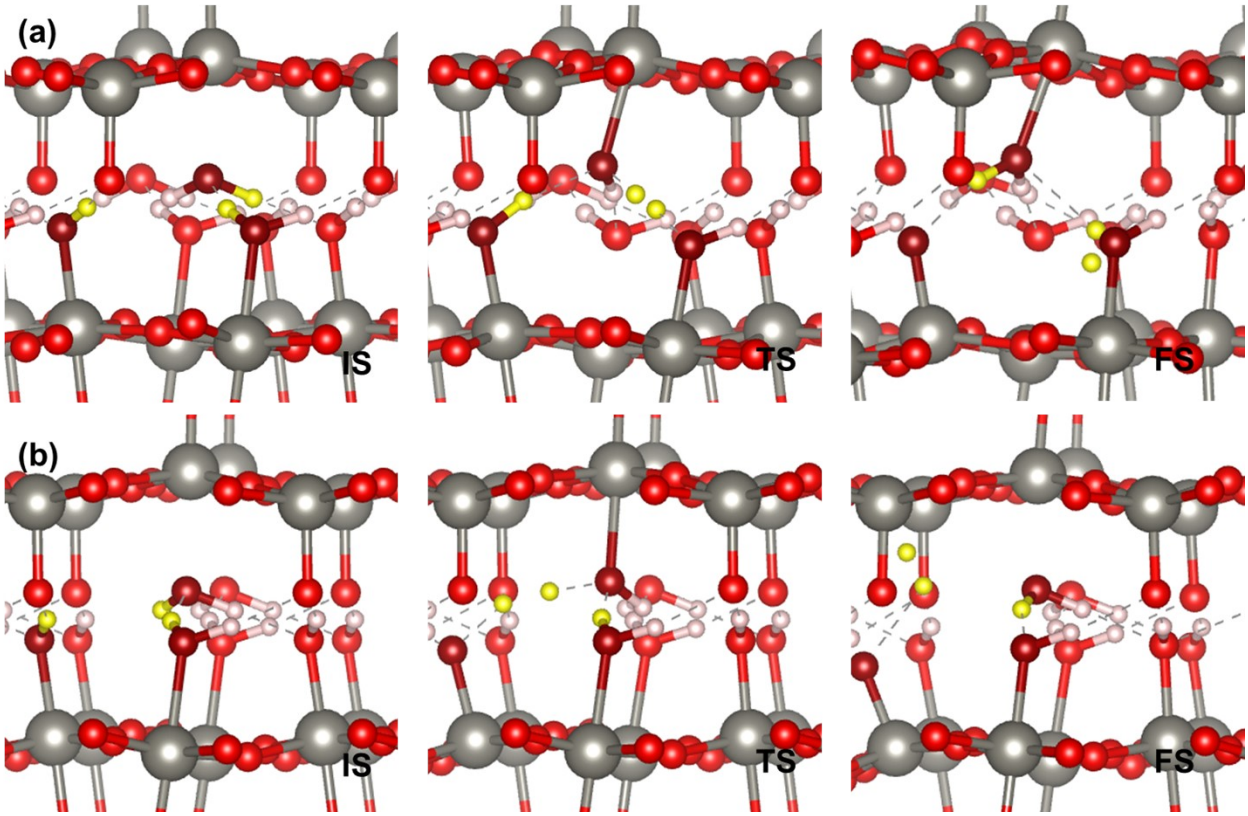

Figure S13. Structural configuration of initial, transition and final states in two additional pathways examined for hydrogen formation within the bulk of $H_{0.5}WO_3 \cdot H_2O$. The free energy of activation barriers are 2.64 eV and 2.25 eV at room temperature, respectively. We investigated the potential pathway of hydrogen formation in $H_{0.5}WO_3 \cdot H_2O$ via hydronium formation (stepwise); however, hydronium itself was found to be unstable in the bulk structure. Hydrogens involved in H_2 formation and the relevant oxygen sites are color-coded in yellow and dark red, respectively.

References:

(1) Cao, C.; Steinrück, H. G.; Shyam, B.; Stone, K. H.; Toney, M. F. In Situ Study of Silicon Electrode Lithiation with X-Ray Reflectivity. *Nano Lett* **2016**, *16* (12), 7394–7401. https://doi.org/10.1021/acs.nanolett.6b02926.

(2) Szymanski, J. T.; Roberts, A. C. The Crystal Structure of Tungstite, $WO_3 \cdot H_2O$. *Can Mineral* **1984**, *22*, 681–688.

(3) Li, Y. M.; Hibino, M.; Miyayania, M.; Kudo, T. Proton Conductivity of Tungsten Trioxide Hydrates at Intermediate Temperature. *Solid State Ion* **2000**, *134*, 271–279.

(4) Woodward, P. M.; Sleight, A. W.; Vogt, T. Structure Refinement of Triclinic Tungsten Trioxide. *Journal of Physics and Chemistry of Solids* **1995**, *56* (10), 1305–1315. https://doi.org/10.1016/0022-3697(95)00063-1.

(5) Hansen, J. N.; Prats, H.; Toudahl, K. K.; Mørch Secher, N.; Chan, K.; Kibsgaard, J.; Chorkendorff, I. Is There Anything Better than Pt for HER? *ACS Energy Lett* **2021**, *6* (4), 1175–1180. https://doi.org/10.1021/acsenergylett.1c00246.

(6) Kibsgaard, J.; Chen, Z.; Reinecke, B. N.; Jaramillo, T. F. Engineering the Surface Structure of MoS2 to Preferentially Expose Active Edge Sites for Electrocatalysis. *Nat Mater* **2012**, *11* (11), 963–969. https://doi.org/10.1038/nmat3439.

(7) Wu, L.; Dzade, N. Y.; Yu, M.; Mezari, B.; Van Hoof, A. J. F.; Friedrich, H.; De Leeuw, N. H.; Hensen, E. J. M.; Hofmann, J. P. Unraveling the Role of Lithium in Enhancing the Hydrogen Evolution Activity of MoS2: Intercalation versus Adsorption. *ACS Energy Lett* **2019**, *4* (7), 1733–1740. https://doi.org/10.1021/acsenergylett.9b00945.

(8) Faber, M. S.; Dziedzic, R.; Lukowski, M. A.; Kaiser, N. S.; Ding, Q.; Jin, S. High-Performance Electrocatalysis Using Metallic Cobalt Pyrite (CoS 2) Micro- and Nanostructures. *J Am Chem Soc* **2014**, *136* (28), 10053–10061. https://doi.org/10.1021/ja504099w.

(9) Cabán-Acevedo, M.; Stone, M. L.; Schmidt, J. R.; Thomas, J. G.; Ding, Q.; Chang, H. C.; Tsai, M. L.; He, H.; Jin, S. Efficient Hydrogen Evolution Catalysis Using Ternary Pyrite-Type Cobalt Phosphosulphide. *Nat Mater* **2015**, *14* (12), 1245–1251. https://doi.org/10.1038/nmat4410.

(10) Li, Y. H.; Liu, P. F.; Pan, L. F.; Wang, H. F.; Yang, Z. Z.; Zheng, L. R.; Hu, P.; Zhao, H. J.; Gu, L.; Yang, H. G. Local Atomic Structure Modulations Activate Metal Oxide as Electrocatalyst for Hydrogen Evolution in Acidic Water. *Nat Commun* **2015**, *6* (1), 8064. https://doi.org/10.1038/ncomms9064.

(11) Luo, Z.; Miao, R.; Huan, T. D.; Mosa, I. M.; Poyraz, A. S.; Zhong, W.; Cloud, J. E.; Kriz, D. A.; Thanneeru, S.; He, J.; Zhang, Y.; Ramprasad, R.; Suib, S. L. Mesoporous MoO3–x Material as an Efficient Electrocatalyst for Hydrogen Evolution Reactions. *Adv Energy Mater* **2016**, *6* (16). https://doi.org/10.1002/aenm.201600528.

(12) Zhang, W.; Li, H.; Firby, C. J.; Al-Hussein, M.; Elezzabi, A. Y. Oxygen-Vacancy-Tunable Electrochemical Properties of Electrodeposited Molybdenum Oxide Films. *ACS Appl Mater Interfaces* **2019**, *11* (22), 20378–20385. https://doi.org/10.1021/acsami.9b04386.

(13) Wu, Z.; Yang, P.; Li, Q.; Xiao, W.; Li, Z.; Xu, G.; Liu, F.; Jia, B.; Ma, T.; Feng, S.; Wang, L. Microwave Synthesis of Pt Clusters on Black TiO2 with Abundant Oxygen Vacancies

for Efficient Acidic Electrocatalytic Hydrogen Evolution. *Angewandte Chemie - International Edition* **2023**. https://doi.org/10.1002/anie.202300406.

(14) Li, Y.; Yu, Z. G.; Wang, L.; Weng, Y.; Tang, C. S.; Yin, X.; Han, K.; Wu, H.; Yu, X.; Wong, L. M.; Wan, D.; Wang, X. R.; Chai, J.; Zhang, Y. W.; Wang, S.; Wang, J.; Wee, A. T. S.; Breese, M. B. H.; Pennycook, S. J.; Venkatesan, T.; Dong, S.; Xue, J. M.; Chen, J. Electronic-Reconstruction-Enhanced Hydrogen Evolution Catalysis in Oxide Polymorphs. *Nat Commun* **2019**, *10* (1). https://doi.org/10.1038/s41467-019-11124-w.

(15) Dickens, P. G.; Hurditch, R. J. X-Ray and Neutron Diffraction Studies of a Tetragonal Hydrogen Bronze H_xWO_3. *Nature* **1967**, *215*, 1266–1267.

(16) Glemser, V. O.; Naumann, C. Kristallisierte Wolframblauverbindungen; Wasserstoffanaloga Der Wolframbronzen H_xWO_3. *ZAAC - Journal of Inorganic and General Chemistry* **1951**, *265*, 288–302. https://doi.org/10.1002/zaac.19512650413.

(17) Wiseman, P. J.; Dickens, P. G. The Crystal Structure of Cubic Hydrogen Tungsten Bronze. *J Solid State Chem* **1973**, *6*, 374–377.

(18) Howard, C. J.; Stokes, H. T. Group-Theoretical Analysis of Octahedral Tilting in Perovskites. *Acta Crystallogr* **1998**, *B54*, 782–789.

(19) Lalik, E.; Drużbicki, K.; Irvine, G.; Gutmann, M.; Rudić, S.; Manuel, P.; Petříček, V.; Krzystyniak, M. Interplay between Local Structure and Nuclear Dynamics in Tungstic Acid: A Neutron Scattering Study. *The Journal of Physical Chemistry C* **2021**. https://doi.org/10.1021/acs.jpcc.1c05121.

(20) Liu, T.; Holzapfel, N. P.; Woodward, P. M. Understanding Structural Distortions in Hybrid Layered Perovskites with the *n* = 1 Ruddlesden–Popper Structure. *IUCrJ* **2023**, *10* (4). https://doi.org/10.1107/S2052252523003743.